

The UV / optical spectra of the type Ia supernova SN 2010jn: A bright supernova with outer layers rich in iron-group elements.

S. Hachinger^{1,2}, P. A. Mazzali^{1,2}, M. Sullivan³, R. S. Ellis⁴, K. Maguire³, A. Gal-Yam⁵,
D. A. Howell^{6,7}, P. E. Nugent⁸, E. Baron^{9,10,11,12}, J. Cooke¹³, I. Arcavi⁵, D. Bersier¹⁴,
B. Dilday^{6,7}, P. A. James¹⁴, M. M. Kasliwal¹⁵, S. R. Kulkarni⁴, E. O. Ofek⁵, R. R. Laher¹⁶,
J. Parrent^{6,17}, J. Surace¹⁶, O. Yaron⁵, E. S. Walker¹⁸

¹*Istituto Nazionale di Astrofisica-OAPd, vicolo dell'Osservatorio 5, 35122 Padova, Italy*

²*Max-Planck-Institut für Astrophysik, Karl-Schwarzschild-Str. 1, 85748 Garching, Germany*

³*Department of Physics (Astrophysics), University of Oxford, Keble Road, Oxford OX1 3RH, UK*

⁴*Cahill Center for Astrophysics, California Institute of Technology, Pasadena, CA 91125, USA*

⁵*Ben-Zvi Center for Astrophysics, Weizmann Institute of Science, 76100 Rehovot, Israel*

⁶*Las Cumbres Observatory Global Telescope Network, Goleta, CA 93117, USA*

⁷*Department of Physics, University of California, Santa Barbara, CA 93106-9530, USA*

⁸*Computational Cosmology Center, Lawrence Berkeley National Laboratory, 1 Cyclotron Rd., Berkeley CA 94720, USA*

⁹*Homer L. Dodge Department of Physics and Astronomy, University of Oklahoma, 440 W Brooks, Norman, OK 73019, USA*

¹⁰*Hamburger Sternwarte, Gojenbergsweg 112, 21029 Hamburg, Germany*

¹¹*Computational Research Division, Lawrence Berkeley National Laboratory, 1 Cyclotron Rd, Berkeley, CA 94720, USA*

¹²*Physics Department, University of California, Berkeley, CA 94720, USA*

¹³*Centre for Astrophysics & Supercomputing, Swinburne University of Technology, Mail H30, PO Box 218, Hawthorn, Victoria 3122, Australia*

¹⁴*Astrophysics Research Institute, Liverpool John Moores University, Twelve Quays House, Egerton Wharf, Birkenhead CH41 1LD, UK*

¹⁵*Observatories of the Carnegie Institution of Science, 813 Santa Barbara St, Pasadena, CA 91101, USA*

¹⁶*Spitzer Science Center, California Institute of Technology, M/S 314-6, Pasadena, CA 91125, USA*

¹⁷*6127 Wilder Lab, Department of Physics & Astronomy, Dartmouth College, Hanover, NH 03755, USA*

¹⁸*Scuola Normale Superiore di Pisa, Piazza dei Cavalieri 7, 56126 Pisa, Italy*

arXiv v1, 2012 Aug 06. The definitive version will be available at www.blackwell-synergy.com.

ABSTRACT

Radiative transfer studies of Type Ia supernovae (SNe Ia) hold the promise of constraining both the time-dependent density profile of the SN ejecta and its stratification by element abundance which, in turn, may discriminate between different explosion mechanisms and progenitor classes. Here we present a detailed analysis of *Hubble Space Telescope* ultraviolet (UV) and ground-based optical spectra and light curves of the SN Ia SN 2010jn (PTF10ygu). SN 2010jn was discovered by the Palomar Transient Factory (PTF) 15 days before maximum light, allowing us to secure a time-series of four UV spectra at epochs from -11 to $+5$ days relative to B -band maximum. The photospheric UV spectra are excellent diagnostics of the iron-group abundances in the outer layers of the ejecta, particularly those at very early times. Using the method of ‘Abundance Tomography’ we have derived iron-group abundances in SN 2010jn with a precision better than in any previously studied SN Ia. Optimum fits to the data can be obtained if burned material is present even at high velocities, including significant mass fractions of iron-group elements. This is consistent with the slow decline rate (or high ‘stretch’) of the light curve of SN 2010jn, and consistent with the results of delayed-detonation models. Early-phase UV spectra and detailed time-dependent series of further SNe Ia offer a promising probe of the nature of the SN Ia mechanism.

Key words: supernovae: general – supernovae: individual (SN 2010jn) – techniques: spectroscopic – radiative transfer

1 INTRODUCTION

Supernovae (SNe) play an important role in many areas of modern astrophysics. In particular, Type Ia SNe (SNe Ia) produce most of

the iron-group elements in the cosmos (Iwamoto et al. 1999), and can be used as ‘standardizable candles’ to probe the expansion history of the universe (e.g. Riess et al. 1998; Perlmutter et al. 1999; Riess et al. 2007; Kessler et al. 2009; Sullivan et al. 2011). Because of their importance, extensive efforts are under way to build a comprehensive observational and theoretical picture of SNe Ia (e.g. Hillebrandt & Niemeyer 2000; Mazzali et al. 2007; Howell 2011; Röpke et al. 2011). A primary aim is to understand the nature and diversity of the explosions and thus to place on a physical ground the empirical calibration procedures that are used to deduce the luminosity of SNe Ia from their light-curve shape (e.g. Phillips 1993; Phillips et al. 1999). Another aim is to determine the progenitor systems of SNe Ia.

One way to improve our understanding of SN Ia physics is to analyse and interpret detailed observations through radiation transport models. A particularly useful technique is that of ‘Abundance Tomography’ (Stehle et al. 2005), where a time-series of SN Ia spectra is modelled and information obtained about the density profile of the SN ejecta and its stratification in terms of element abundances. This makes it possible to describe the mode of explosion and possibly to discriminate among different progenitor scenarios. Many detailed spectral time series for SNe Ia have become available in the last decade, but most of them are restricted to optical wavelengths. The ultraviolet (UV) spectrum of SNe Ia is shaped by iron-group elements, which dominate line-blocking and fluorescence effects (Pauldrach et al. 1996; Mazzali 2000). Thus, series of UV spectra are invaluable diagnostics for iron-group abundances and ejecta densities in different zones of the SN. These in turn are indicators for basic explosion properties such as burning efficiency or explosion energy (Iwamoto et al. 1999). Extensive work on UV spectra of SNe Ia has been carried out in the last few years (e.g. Ellis et al. 2008; Foley et al. 2008; Sauer et al. 2008; Cooke et al. 2011; Walker et al. 2012; Maguire et al. 2012), however the focus has usually been to obtain a single spectrum per SN. Both observations and models indicate that even SNe Ia with similar optical spectra can be very different in the UV (Lentz et al. 2000; Ellis et al. 2008; Sauer et al. 2008; Walker et al. 2012).

Here we present observations and models of the SN Ia 2010jn (PTF10ygu). The SN was discovered by the Palomar Transient Factory (PTF) only a few days after explosion, which allowed a detailed spectral time series to be obtained, including UV data from the *Hubble Space Telescope*. The combined optical-UV spectra make it possible to conduct an analysis of the SN in unprecedented detail. Abundance Tomography was performed based on density profiles resulting from single-degenerate Chandrasekhar-mass explosion models. These models (cf. e.g. Hillebrandt & Niemeyer 2000) assume that SNe Ia are the explosion of an accreting carbon-oxygen (CO) white dwarf (WD). We used both the fast-deflagration model W7 (Nomoto et al. 1984; Iwamoto et al. 1999), which has been shown to match average SNe Ia (Stehle et al. 2005; Tanaka et al. 2011), and a more energetic delayed-detonation model (WS15DD3, Iwamoto et al. 1999). The latter model assumes that the combustion flame, which initially propagates subsonically (deflagration), becomes supersonic (detonation) at some point (Khokhlov 1991). Based on the quality of the fits, we suggest that the latter model is a more realistic description of SN 2010jn.

The paper starts with a report on the observations and a presentation of the observed spectra, which were obtained from -13 d to $+5$ d (time in the SN rest frame) with respect to maximum light in the rest-frame *B*-band (Section 2). Afterwards, we discuss our models. We lay out the objectives, methods and assumptions (Sections 3.1 – 3.4). Synthetic spectra are presented and the inferred

abundance profiles are discussed (Sections 3.5, 3.6). Finally, results are summarised and conclusions are drawn (Section 4).

2 OBSERVATIONS, DATA REDUCTION AND PHOTOMETRIC PROPERTIES

SN 2010jn (PTF10ygu) was discovered on 2010 October 12 UT by the Palomar Transient Factory (PTF; Law et al. 2009; Rau et al. 2009) using the Palomar 48-in telescope (P48), through the citizen science project ‘Galaxy Zoo: Supernova’ (Smith et al. 2011)¹. The SN was found at a magnitude of $r \sim 19.2$ in the Sbc galaxy NGC2929, at a heliocentric redshift of $z = 0.02505$ (CMB-frame redshift of 0.02602, yielding a distance modulus $\mu = 35.2$ mag²), and a spatial position of RA 09:37:30.3, Dec. +23:09:33 (J2000). Only a marginal detection was present in data from the previous night, and no detection in data taken on 2010 October 08. Because of the relatively low redshift and apparent early discovery, a classification spectrum was triggered using the Gemini-N telescope and the Gemini Multi-Object Spectrograph (GMOS; Hook et al. 2004) on 2010 October 13 (program ID GN-2010B-Q-13). This revealed an early SN Ia at about 15 days before maximum light.

Based on this classification, four epochs of UV observations of this SN were triggered with the *Hubble Space Telescope* (*HST*) using the Space Telescope Imaging Spectrograph (STIS) as part of the cycle 18 program 12298: ‘Towards a Physical Understanding of the Diversity of Type Ia Supernovae’ (PI: Ellis). A spectral monitoring campaign with ground-based telescopes was also commenced. Multi-colour light curves were obtained with the Liverpool Telescope (LT; Steele et al. 2004) using RATCam and with the Faulkes Telescope North (FTN).

An observing log for the *HST* data can be found in Table 1. We use two observing modes, both with a $0.2''$ slit: the G430L/CCD on all four epochs (giving coverage from ~ 2900 Å out to ~ 5700 Å), and the G230LB/CCD (with nominal coverage from ~ 2000 Å to ~ 3000 Å). Unfortunately, the more sensitive G230L/MAMA mode was not available as the MAMA was offline. Since the intrinsic UV flux of SNe Ia below ~ 2700 Å is low, the G230LB/CCD observations only provide useful data redwards of this wavelength.

We also make use of five ground-based optical spectra, taken with Gemini-N with GMOS and the William Herschel Telescope (WHT) with the Intermediate dispersion Spectrograph and Imaging System (ISIS). With GMOS, we used the B600 grating with a central wavelength of 450nm, and the R400 grating with a central wavelength of 750nm. With ISIS, we used the R158R (red arm) and R300B (blue arm) gratings, together with the 5300 dichroic. Again, details can be found in Table 1. At the earliest epoch we analyse (-12.9 d), only an optical spectrum is available. At all other epochs, we use both *HST* and ground-based spectra, taken within 12 hours of each other.

2.1 Data reduction

2.1.1 Spectra

The treatment of the *HST* spectra is described in Maguire et al. (2012). Briefly, the spectra were downloaded from the *HST* archive

¹ PTF10ygu discoverers: Peter Woolliams, tracey, Graham Dungworth, Ipspieler, John P Langridge, Elisabeth Baeten, Tomas Raudys, adam elbourne, Robert Gagliano

² A Hubble constant $H_0 = 72$ km s⁻¹ Mpc⁻¹ is used throughout.

Table 1. Log of the spectroscopic observations of SN 2010jn / PTF10ygu.

Calendar date of observation (UT)	Date of obs. (MJD)	Phase (days) ^a	Telescope	Instrument configuration	Exposure time (s)
Oct 13	55482.6	−12.9	Gemini-N	GMOS/B600/R400	450
Oct 16	55485.0	−10.5	<i>HST</i>	STIS/G430L/CCD	2175
Oct 16	55485.6	−10.0	Gemini-N	GMOS/B600/R400	450
Oct 20	55489.8	−5.9	<i>HST</i>	STIS/G430L/CCD	2175
Oct 20	55489.9	−5.8	<i>HST</i>	STIS/G230LB/CCD	4920
Oct 21	55490.6	−5.1	Gemini-N	GMOS/B600/R400	450
Oct 26	55495.4	−0.4	<i>HST</i>	STIS/G430L/CCD	2175
Oct 26	55495.5	−0.3	<i>HST</i>	STIS/G230LB/CCD	7665
Oct 27	55496.6	+0.8	Gemini-N	GMOS/B600/R400	450
Oct 31	55500.7	+4.8	<i>HST</i>	STIS/G430L/CCD	2175
Nov 01	55501.2	+5.3	WHT	ISIS/R300B/R158R	900

^adays in the SN rest frame relative to maximum light in the rest-frame *B*-band

using the on-the-fly reprocessing (OTFR) pipeline, giving fully calibrated and extracted 1-D spectra, where the reduction and extraction is optimised for point sources. The OTFR pipeline uses the latest calibration files and data parameters to perform initial 2-D image reduction such as image trimming, bias and dark current subtraction, cosmic-ray rejection, and flat-fielding. It then performs wavelength and flux calibrations. We applied further cosmic-ray removal and hot-pixel masking by hand. The ground-based spectra were reduced using standard IRAF procedures (see acknowledgements), including bias subtraction, flat-fielding, wavelength calibration, flux calibration, and telluric feature removal. The techniques used were similar to those described in Ellis et al. (2008).

For all epochs except the first one we combined the various spectra available (i.e., one or two *HST* spectra and one ground-based spectrum). We used *HST* data below ~ 5500 Å, and ground-based data above. In each case, we matched the spectra in the overlap region using the *HST* spectrum as reference. The resulting four optical/UV spectra analysed here sample the SN in regular time intervals of ~ 5 days. They are publically available through the WISEREP archive³ (Yaron & Gal-Yam 2012). We have corrected all final 1-D spectra for Milky Way extinction using $R_V = 3.1$, a colour excess of $E(B - V)_{MW} = 0.03$ from the dust maps of Schlegel et al. (1998), and the Milky Way dust extinction law of Cardelli, Clayton & Mathis (1989).

2.1.2 Light curves

Light curves were produced from the P48 *R* and LT/FTN *gri* photometric data using difference imaging; full details can be found in Maguire et al. (2012). In all cases, a reference image with no SN light is produced, and subtracted from each image in which the SN is present by matching the point-spread functions (PSFs) of the images. In the case of the P48 data, this reference image was constructed using data from before the SN exploded; for the LT/FTN data the reference image was taken 18 months after the SN was first detected, by which time the SN flux was $< 1\%$ of its peak value. We measure the SN photometry using a PSF fitting method. In each image frame (prior to subtraction), the PSF is determined from nearby field stars. This average PSF is then fit at the position of the SN in the difference image. Each pixel is weighed according to Poisson statistics, yielding a SN flux and flux error.

The light curves are flux-calibrated to the Sloan Digital Sky

Survey (SDSS) Data Release 8 (DR8) photometric system, close to the AB system (Oke & Gunn 1983), using stars in the field-of-view of the SN. We generally follow the procedures outlined in Ofek et al. (2012). In the LT/FTN data (*g*, *r* and *i* filters), the colour terms to the SDSS system are very small. The P48 colour term is larger, and we include colour, airmass, and colour-airmass terms. The r.m.s. of the colour term fits is $\simeq 0.02$ mag (with a colour term in $r - i$ of ~ 0.22 mag), although we present magnitudes in the natural P48 system and do not apply this colour term to our photometry. Finally, we fit the same PSF used for the SN flux measurement to the calibrating field stars. We then use these data to apply aperture corrections to the SN photometry on an image-by-image basis. These corrections are small ($< 3\%$) and account for the difference between the fixed aperture in which the calibration is performed, and the PSF-fit in which the SN photometry is measured. In Fig. 1, our observed light curve data are presented.

2.2 Photometric properties

Estimating the peak luminosity of SNe Ia in a given rest-frame bandpass requires an interpolation between observed data points at the time of maximum light, followed by a *k*-correction (e.g. Nugent et al. 2002; Hsiao et al. 2007) back to the standard rest-frame filter of interest using a time series spectral energy distribution (SED). We fit the observed photometry for SN 2010jn using the SiFTO light curve fitter (Conley et al. 2008) developed for SNIa cosmology studies.

SiFTO works in flux space, manipulating a SED template and synthesizing an observer-frame light curve from a given spectral time-series in a set of filters at a given redshift. These template light-curves are then fit to the data, adjusting the time-axis of each of the template light curves by a common ‘stretch’ (*s*) factor (where the input SED time-series template is defined to have $s = 1$). The normalisations in the observed filters are independent, i.e., the absolute colours of the SED template used in the fit are not important and do not influence the fit. The result is a set of maximum-light, observer frame magnitudes, and a stretch factor.

Once this observer-frame SiFTO fit is complete, it can be used to estimate rest-frame magnitudes in any given set of filters, provided there is equivalent observer-frame filter coverage. This is performed by adjusting (or ‘warping’) the template SED to have the correct observed colours from the SiFTO fit, correcting for extinction along the line of sight in the Milky Way, de-redshifting, and integrating the resultant rest-frame SED through the required filters. This process is essentially a cross-filter *k*-correction, with

³ <http://www.weizmann.ac.il/astrophysics/wiserep/>

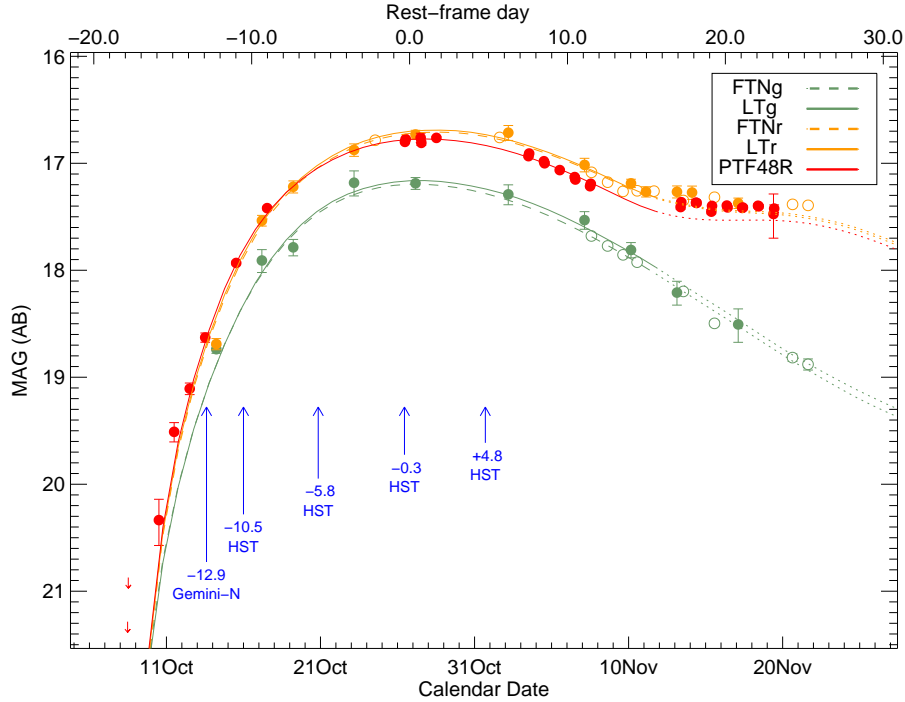


Figure 1. The light curve of SN 2010jn / PTF10ygu in apparent AB magnitudes. The photometry has been taken from the Palomar 48-in telescope (P48) in R (solid red circles), the Liverpool Telescope (LT; solid green and orange circles) and Faulkes Telescope North (FTN; open green and orange circles) in g and r . No correction for extinction in the Milky Way or the SN host galaxy has been applied. Over-plotted is a SiFTO light curve fit (solid lines for P48 and LT data, and dashed lines for FTN data). Only data points up to +15 days past the (rest-frame) B -band maximum are used in the fit. The template lines are dotted after this phase and show the predicted evolution at later phase; however the SiFTO template in R/r is not expected to reproduce the observed secondary maximum. The arrows mark the epochs (given relative to the rest-frame B -band maximum) of the four *HST* spectra.

the advantage that all the observed data can contribute to the overall SED shape. We only use P48 and LT data (which have a wider phase coverage than the FTN data) for this colour warping; SiFTO does not handle filters that are very close in wavelength in this process (e.g., LT g and FTN g). However, all the FTN data are used to constrain the stretch and time of maximum light.

Our SiFTO light curve fit is shown in Fig. 1. The fit is reasonable: the χ^2 of the fit is 27 for 43 degrees of freedom. Maximum light in the rest-frame B -band was on MJD 55495.8 \pm 0.1, or UT 2010-10-26.8, i.e., the SN was discovered some 15 days before maximum light, as expected from the analysis of the first Gemini spectrum. The stretch is 1.06 ± 0.02 , corresponding to $\Delta m_{15}(B) = 0.9$ mag – the evolution of the light curve is slightly slower than for a typical SNIa. We measure peak rest-frame absolute magnitudes at the time of B -band maximum light of $M_B = -17.94 \pm 0.04$ and $M_V = -18.36 \pm 0.02$, and a SiFTO colour C (broadly equivalent to $B - V$ at B -band maximum light) of 0.42 ± 0.03 . We take the BV filter responses from Bessell (1990), and these magnitudes are in the Vega system converted from the (near)-AB system in which the photometry is measured. The uncertainties are based on statistical errors propagated through the light curve fit. This indicates that PTF10ygu was fainter than its light curve stretch would indicate, and redder than a normal SNIa, both presumably the result of extinction by dust (see Sec. 3.4).

We can estimate the (B -band) rise time of the SN (τ_r , defined here as the time from explosion to B maximum) from the very early P48 data, independently of the SiFTO light curve fit. To this end, we measure the explosion epoch by fitting the P48 R data at early epochs ($\lesssim 5$ d after discovery) using the analytical equation $f(t) = \alpha \times (\tau + \tau_r)^2$ (‘fireball model’; Riess et al.

1999; Goldhaber et al. 1998). Here, $\tau = t_o/(1+z)$ where t_o is the (observer-frame) epoch relative to B maximum, and α is a normalising constant. This yields $\tau_{r,\text{fire}} = 18.6 \pm 0.3$ d. Leaving the exponent as a free fit parameter [$f(t) = \alpha \times (\tau + \tau_r)^\eta$], we obtain a best-fit rise time of $\tau_{r,\text{free}} = 19.1 \pm 1.2$ d with an exponent of $\eta = 2.3 \pm 0.6$, slightly deviating from the value of $\eta = 1.8$ derived by Piro (2012). Enforcing his $\eta = 1.8$ gives $\tau = 18.3 \pm 0.3$ d. Our light curve template (stretch 1.0) has a rise time of ~ 17 d. Scaling it to the stretch of SN 2010jn (i.e. to the higher opacity in such a slowly-declining object), we obtain an estimate of $\tau_{r,\text{LCfit}} \sim 18.2$ d, slightly shorter than the values inferred from the early rise (and indicating the very early-time SiFTO templates may not match the data well). Our spectral models, on the other hand, lead us to prefer a somewhat higher value (~ 20 d; Sec. 3.4, Appendix A), indicating some tension between the rise time inferred from the early-time data with $\eta = 2$, and the rise time favoured by spectral modelling.

3 SPECTRA AND MODELS

3.1 Objectives

With the aim of obtaining a comprehensive picture of SN 2010jn, we now derive ejecta models from the observed spectra. We use the method of Abundance Tomography (Stehle et al. 2005): an ejecta model is set up, where the density distribution is that of an explosion model, but the abundances are left as ‘free’ parameters. Synthetic spectra are then calculated from this abundance/density model and the abundances are optimised so as to match the observations with the synthetic spectra as closely as possible (cf.

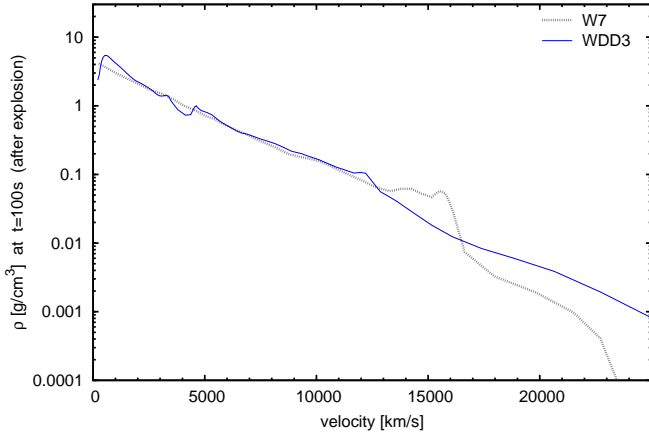


Figure 2. W7 and WS15DD3 (short WDD3) density profiles (Iwamoto et al. 1999) used for our tomography experiments.

Sec. 3.2.2). Our code (Sec. 3.2.1) was successfully applied to obtain spectral models for single UV spectra of various SNe Ia (Sauer et al. 2008; Walker et al. 2012). We profit from this experience here, and perform for the first time tomography of a SNe Ia including UV spectra, deriving a detailed abundance stratification. The UV spectra, especially those taken as early as -10.5 or -5.8 d, when the outer layers leave their imprint in the spectrum, allow us to constrain iron-group abundances in the outer and intermediate layers of the SN. We perform the tomography for different explosion models. Thus, the quality of the spectral fits can be compared. Furthermore, for each explosion model we can check the consistency of the explosive nucleosynthesis, as calculated in the hydrodynamic model, with the abundances we derive from the spectral fits. Finally, we can judge which hydrodynamic model offers a more realistic representation of SN 2010jn.

Two different explosion models are tested in this paper: the ‘fast deflagration’ model W7 (Nomoto et al. 1984; Iwamoto et al. 1999) and the ‘delayed-detonation’ model WS15DD3 (Iwamoto et al. 1999). Both represent single-degenerate Chandrasekhar-mass explosions. Their density distributions are shown in Fig. 2. The W7 model has been shown to provide excellent fits to light curves and spectra of average as well as lower-than-average luminosity SNe Ia (e.g. Stehle et al. 2005; Mazzali et al. 2008; Tanaka et al. 2011). Although its physical foundations are now known not to be realistic, as it assumes that a deflagration flame with parametrised propagation speed burns the star, its density distribution is representative of most explosion models, except for the outermost layers, so we use it as a benchmark. WS15DD3, a delayed-detonation model, is more physically consistent, and it has a higher explosion kinetic energy and ^{56}Ni mass, both of which turn out to be more appropriate for the (intrinsically) luminous SN 2010jn.

3.2 Methods

We briefly describe the code which we use to calculate the synthetic spectra and the method of Abundance Tomography.

3.2.1 Monte-Carlo radiative transfer code

We use a Monte-Carlo radiative transfer code (Abbott & Lucy 1985, Mazzali & Lucy 1993, Lucy 1999, Mazzali 2000 and Stehle et al. 2005) in spherical symmetry to compute the formation

of the spectrum in an expanding SN envelope at a given epoch. The code assumes a sharp photosphere from which radiation is emitted, and computes the interaction of the photons with the expanding SN ejecta (‘atmosphere’). An initial density profile, usually the outcome of a hydrodynamic calculation, is used to calculate the densities within the atmosphere at the epoch required. This takes advantage of the fact that the ejecta are in a state of homologous, force-free expansion at the epochs relevant here (e.g. Röpke & Hillebrandt 2005), i.e., for each particle within the ejecta, $r = v \times t$ is a good approximation, where r is the distance from the centre, t the time from explosion and v the velocity of homologous expansion. Radius and velocity can therefore be used interchangeably as spatial coordinates.

The outward-flowing radiation at the photosphere, which is characterised by a velocity v_{ph} , is assumed to be a Planck continuum at a temperature T_{ph} [$I_{\nu}^{+} = B_{\nu}(T_{\text{ph}})$]. Although this is a relatively rough approximation (Bongard et al. 2008), especially at late times and in SNe where line opacity dominates (e.g. Hachinger et al. 2009, and it can result in a mismatch in the overall flux in the red and infrared, it has only minor consequences on the determination of the abundances from prominent spectral lines.

We simulate the propagation of the emitted photons through the envelope, considering ‘photon packets’ which undergo Thomson scattering and bound-bound processes. The latter processes are treated in the Sobolev approximation, and a good approximation to the bound-bound emissivity is ensured by a downward branching scheme. The construction of the simulation enforces radiative equilibrium (Lucy 1999). When packets are scattered back into the photosphere, they are considered to be re-absorbed and do not contribute to the output luminosity. An essential feature of the code is the consistent determination of a stationary state of the radiation field and of the excitation/ionisation structure of the plasma. To this end, a modified nebular approximation (Mazzali & Lucy 1993; Mazzali 2000) is used to calculate the gas state from a radiation temperature T_R and a dilution factor W cell per cell. The gas state and the radiation field are iterated in turn until the T_R values within the atmosphere are converged to the per cent level. The temperature at the photosphere, T_{ph} , is automatically adjusted in these cycles so as to match a given bolometric output luminosity L_{bol} , compensating for the re-absorption of packets. Finally, the emerging spectrum is not calculated from packet counts, which would introduce additional ‘Monte-Carlo noise’, but rather via a formal integral, using a source function from the packet statistics (Lucy 1999).

3.2.2 Abundance Tomography

For an assumed density profile we model a series of spectra, inferring an optimum abundance stratification. This process of ‘abundance tomography’ (Stehle et al. 2005) is based on the idea that the opaque core of the expanding ejecta shrinks with time (in v space). In other words, the photosphere recedes, and deeper and deeper layers become visible and influence the spectral lines.

From the earliest spectrum available we can obtain a photospheric velocity and abundances within the outer ejecta such that the synthetic spectrum matches the observed one. The next observed spectrum will still show absorption by the material in the outer zone, but additional layers, which only now are above the photosphere, also contribute to the absorption. Keeping the previously inferred abundance values in the outer layers, the abundances in the newly exposed layers and a new photospheric velocity can be inferred. We continue this with later spectra. In some cases, abundances in the outer layers need to be revised in order to optimize

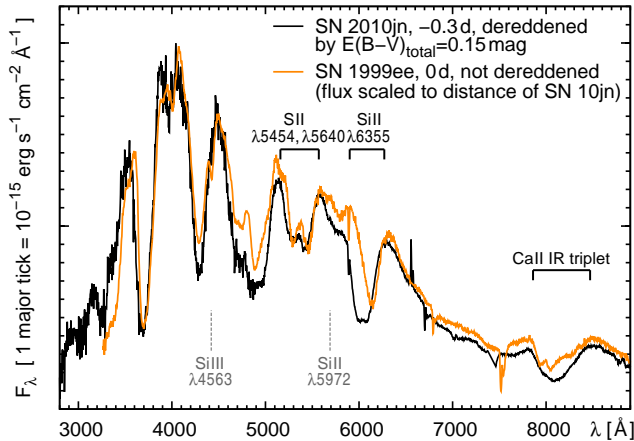


Figure 3. Spectra of SN 2010jn (this work, black line) and SN 1999ee (Hamuy et al. 2002, orange/grey line) around maximum light. The spectrum of SN 1999ee is displayed as observed, but has been multiplied by a factor to account for the difference in distance towards the two SNe ($\Delta\mu \sim 1.7$ mag from NED – see acknowledgements). The spectrum of SN 2010jn has been de-reddened by a total $E(B - V)$ of 0.15 mag, and is then seen to coincide nicely with that of SN 1999ee. The spectral features discussed in the text are marked (features missing in SN 2010jn in grey with dashed marks).

the fit to later spectra. In this case the entire spectral sequence is iterated in order to determine a consistent abundance distribution.

3.3 Some general characteristics of SN 2010jn

SN 2010jn had a very broad light curve, corresponding to a high ^{56}Ni mass, but it was a spectroscopically normal SNIa. It is in fact a close analogue of SN 1999ee [Hamuy et al. (2002); see maximum-light optical spectra in Fig. 3] rather than of SN 1991T (e.g. Filippenko et al. 1992) or SN 1999aa (Garavini et al. 2004); all of which, however, share similar light-curve properties.

The UV flux in SN 2010jn is low, as in other SNe Ia, indicating significant line blocking. The optical P-Cygni absorption features (Fig. 3) of Ca II (IR triplet) and Si II ($\lambda 6355$) show strong high-velocity features (HVF). Although HVFs are common in SNe Ia at early times (Mazzali et al. 2005), those in SN 2010jn stand out by their strength and high velocities (Table 2), similar to those found in SN 1984A (Barbon et al. 1989). Only around B maximum do the HVFs vanish.

Both Si III $\lambda 4563$ and Si II $\lambda 5972$ are very weak or absent in SN 2010jn (Fig. 3). The Si III $\lambda 4563$ feature is characteristic for SNe Ia with high temperature, while Si II $\lambda 5972$ is strongest in low-temperature objects (Nugent et al. 1995; Hachinger et al. 2008). The weakness of both indicates a small abundance of intermediate-mass elements (IME, $9 \leq Z \leq 20$), which is typical of luminous SNe (Mazzali et al. 2007). Only the intrinsically strong Si II $\lambda 6355$ line remains prominent.

3.4 The rise time and reddening of SN 2010jn

Since our code requires an epoch and a luminosity for each model spectrum as input, we need to make assumptions about the B -band rise time of the SN and the reddening.

The B -band rise time τ_r (cf. Sec. 2.2) is necessary to calculate the time from explosion t for each of the observed spectra. The spectral models presented here assume a rise time of 20 d. We

have created tomography models for different values of the rise time (Appendix A), and find that a shorter rise time would imply higher (and probably unrealistic) iron-group abundances in the outer ejecta. This longer rise time implies that the SN after explosion has a ‘dark phase’ longer than predicted by the τ^2 model.

The reddening of SN 2010jn can be estimated in various ways. We have been able to measure the equivalent width of the host-galaxy Na I D line in our observed low-resolution spectra (2.1 Å on average). Thus, we can estimate the host-galaxy reddening using the more conservative (lower-reddening) relation of Turatto et al. (2003):

$$E(B - V) [\text{mag}] = EW(\text{Na I D}) [\text{\AA}] \times 0.16 - 0.01.$$

Including galactic reddening, we arrive at a total reddening $E(B - V)_{\text{total}} = 0.35$ mag⁴ with this method. Since $EW(\text{Na I D})$ in low-resolution spectra may be a relatively uncertain proxy for extinction (Blondin et al. 2009; Poznanski et al. 2011) we obtained further independent estimates.

We can infer the reddening of SN 2010jn relative to a bright SN with similar light curve shape, SN 1999ee ($\Delta m_{15}(B) = 0.95$; Hamuy et al. 2002). Comparison of the spectrum of SN 2010jn at -0.2 d and a maximum-light spectrum of SN 1999ee (Fig. 3) suggests a reddening difference of $\Delta E(B - V)_{\text{total}} \sim 0.15$ mag. Sasdelli (2011) modelled SN 1999ee in detail and found that it was most probably reddened by $E(B - V)_{\text{total}} = 0.26$ mag. Assuming that the SNe are almost identical, this gives a reddening of $E(B - V)_{\text{total}} \sim 0.41$ mag for SN 2010jn.

Finally, our light curve fits give a peak optical colour of $B - V = 0.42$ mag (Sec. 2.2), which can also be taken as an indicator of extinction.

As the three extinction estimates are reasonably consistent with one other, we use their average,

$$E(B - V)_{\text{total}} = 0.39 \text{ mag}.$$

3.5 Models based on the W7 density distribution

We begin by computing synthetic spectra using W7, in order to compare the results for SN 2010jn with those obtained for other SNe [SN 2002bo, Stehle et al. (2005); SN 2003du, Tanaka et al. (2011); SN 2004eo, Mazzali et al. (2008)]. Since SN 2010jn was more luminous than all these SNe, differences in the results may be expected.

Our best-fit synthetic spectra for SN 2010jn based on the W7 model are shown in Fig. 4 together with the observations. We first discuss the spectral fits, then we point out some major shortcomings of the W7-based model. Finally, we show and discuss the abundance stratification we infer using the W7 density.

3.5.1 Spectral models

The first spectrum we model has an epoch of 12.9 d before B -band maximum, i.e. 7.1 d after explosion (for $t_r = 20$ d). The model luminosity is $L_{\text{bol}} = 0.7 \times 10^9 L_{\odot}$. The spectrum shows all lines characterising a typical SNIa in the photospheric phase. This indicates that not only O, but also IME ($\sim 33\%$ by mass) and some iron are

⁴ For low redshifts, such as that of SN 2010jn, galactic and host extinction values can simply be added up to obtain the total reddening.

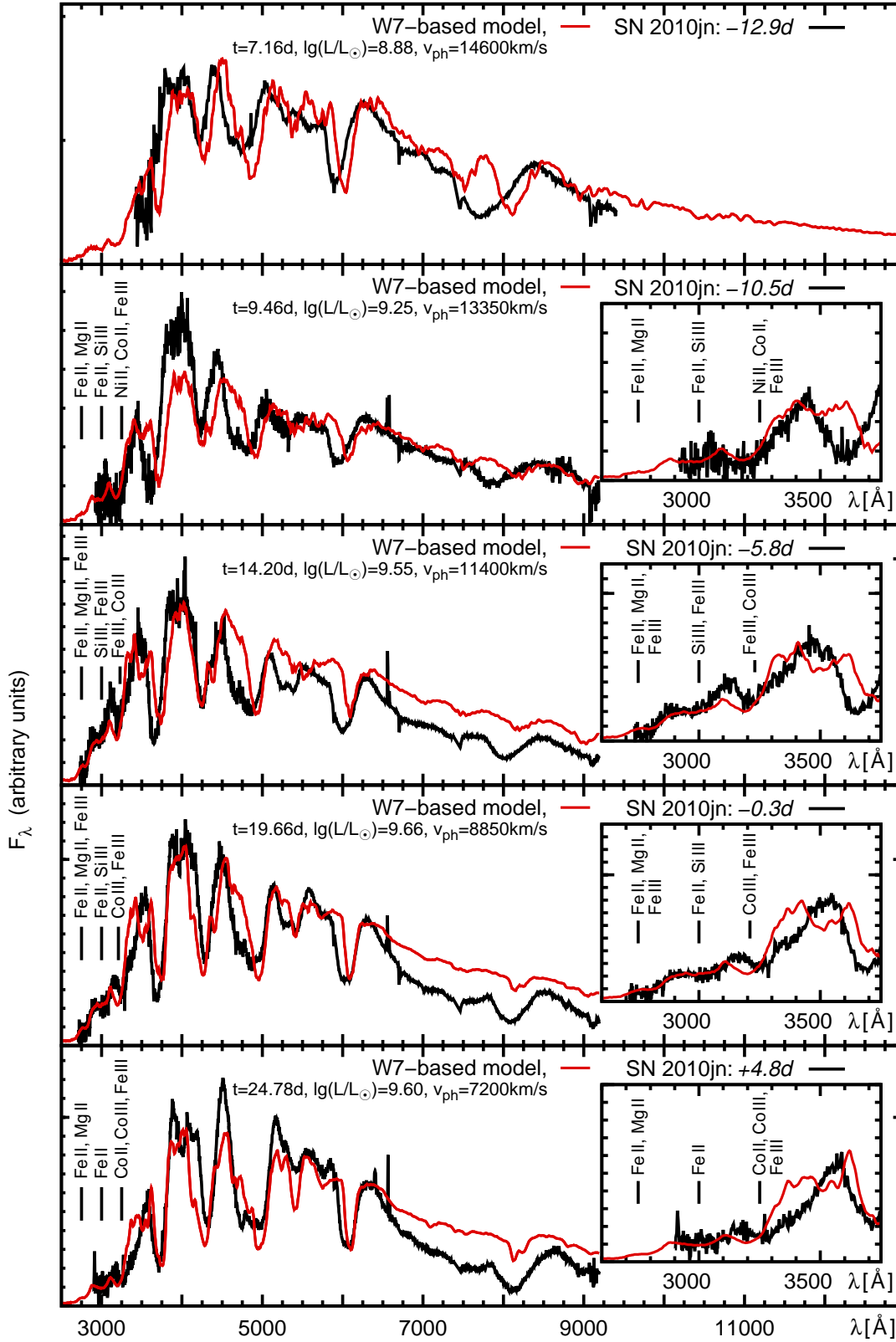


Figure 4. 10jn-W7 model sequence, based on the W7 density profile (red lines). The observed spectra are shown in black for comparison; insets show the UV in more detail. Observations and models are shown de-redshifted (i.e. in the SN's rest frame); no correction for host-galaxy reddening has been applied to the observed spectra [i.e. the models have been reddened by $E(B - V)_{\text{host}} = 0.36$ mag]. For the most prominent UV features, the respective ions dominating the absorption in our model are given (in order of importance). Note that Cr and Ti cause significant quasi-continuous absorption by a large number of weak lines, which are not reported here.

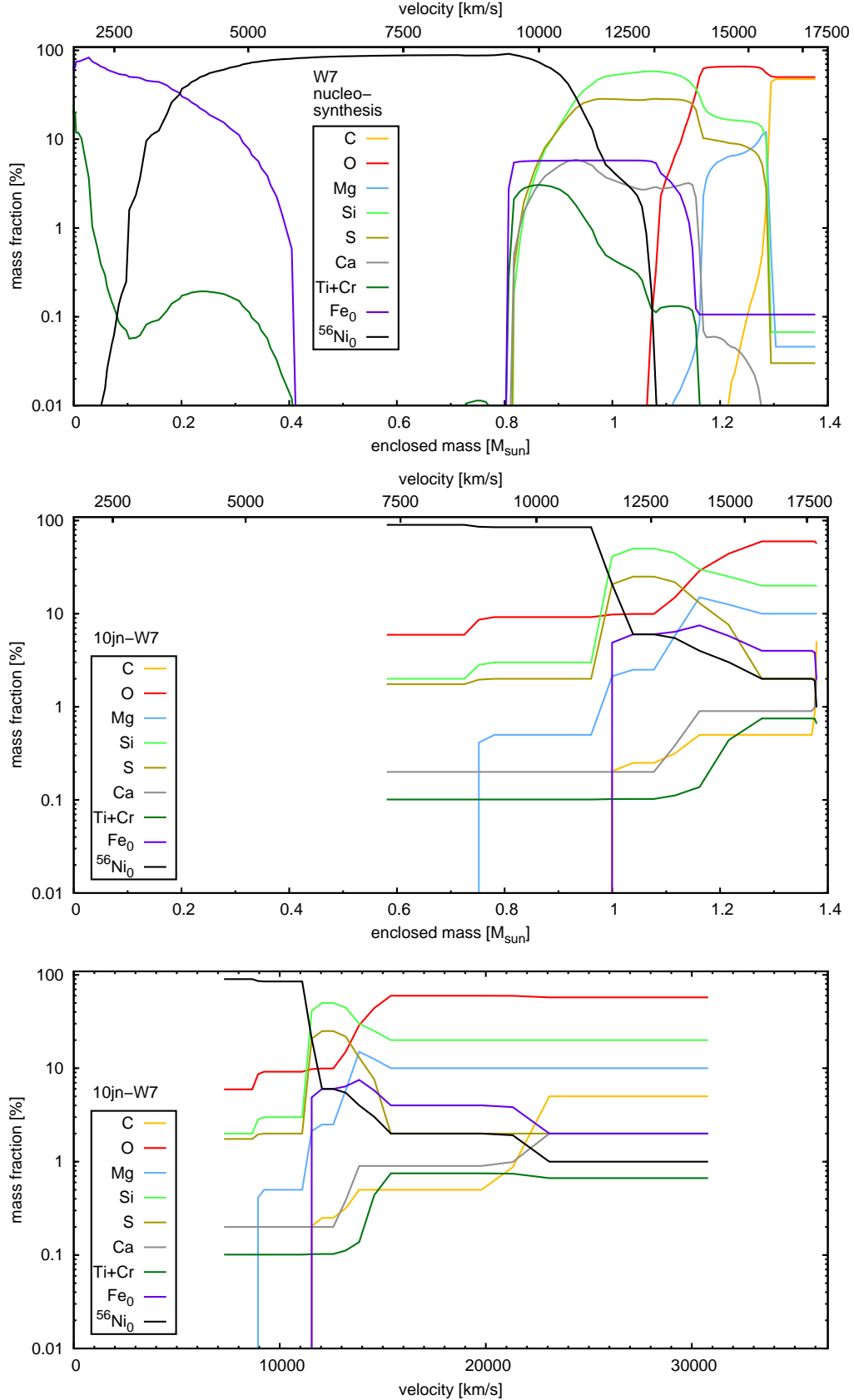


Figure 5. Abundances of W7 nucleosynthesis calculations (Iwamoto et al. 1999, *top panel*, plotted in mass space) vs. Abundance Tomography of SN 1010jn, based on the W7 density profile (10jn-W7 model – *middle panel*: in mass space; *lower panel*: in velocity space). The C abundance in our model is an upper limit, as no C feature is present in the observations. The Ni/Co/Fe abundances are given in terms of the mass fractions of ^{56}Ni and stable Fe at $t = 0$ [$X(^{56}\text{Ni}_0)$, $X(\text{Fe}_0)$]; in our spectral models, no stable Ni or Co and no radioactive Fe are assumed to be present.

Table 2. Velocities of HVFs in SN 2010jn / PTF10ygu. The values given for each feature correspond to the blueshift of the point of deepest absorption. While in Si II $\lambda 5640$, this point normally corresponds to absorption near the photosphere, in Si II $\lambda 6355$ and the Ca II IR feature it is determined by a high-velocity component before maximum. In the later spectra, a photospheric and a HVF component can be distinguished in Si II $\lambda 6355$.

Calendar date (UT)	rest-frame phase (days)	$v(\text{Ca II } \lambda \sim 8600)$ (km s ⁻¹)	$v(\text{Si II } \lambda 6355)$ (km s ⁻¹)	$v(\text{Si II } \lambda 5640)$ (km s ⁻¹)
Oct 13	-12.9	35000	23000	19000 ^a
Oct 16	-10.5	28000	20000	18000 ^a
Oct 20 / 21	-5.8	22000	18000	13000 ^a
Oct 26 / 27	-0.3	19000	17500 / 14000 ^a	12000 ^a
Oct 31 / Nov 1	+4.8	17000	17000 / 13500 ^a	11500 ^a

^a values refer to photospheric absorption

present above the photosphere, which is located at 14600 km s⁻¹ in our model. The observed lines show high blueshifts, which cannot be reproduced by the W7-based model as it lacks high-velocity material. The absorption troughs at $\sim 4300\text{\AA}$ and $\sim 4700\text{\AA}$, which are both due to a mix of Fe and IME lines, serve as diagnostics for the Fe content in the absence of UV data⁵.

At 10.5 d before *B*-band maximum, the W7-based model has a bolometric luminosity of $L_{\text{bol}} = 1.8 \times 10^9 L_{\odot}$ and a photospheric velocity of 13350 km s⁻¹. The temperature of the photospheric black-body spectrum has risen from $T_{\text{ph}} = 11160\text{ K}$ (at -12.9 d) to $T_{\text{ph}} = 12870\text{ K}$. The low UV flux is indicative of efficient line blocking, and requires significant iron-group abundances in the photospheric layer [$X(^{56}\text{Ni}) \sim 4\%$, $X(\text{Fe}_0) \sim 8\%$ and $X(\text{Cr}) \sim 0.1\%$ at the photosphere]⁶. Reverse-fluorescence processes, induced by iron-group elements and IME in the outer layers, actually enhance the UV flux in SNe Ia (Mazzali 2000). In higher-luminosity models such as the ones for SN 2010jn, however, Fe-group elements also have a strong absorbing effect in the UV except for some opacity windows (Walker et al. 2012). Additionally, the radiation field in these models is bluer, disfavoring reverse fluorescence. The two prominent UV absorption features in the -10.5 d model ($\sim 3000\text{\AA}$ and $\sim 3200\text{\AA}$) are mostly due to Fe II and Ni II/Co II lines, respectively. At $\lesssim 2900\text{\AA}$, the UV flux is depressed by Fe II and Mg II lines (and other lines further bluewards). As the $\sim 3200\text{\AA}$ feature is dominated by Ni II and Co II lines, we could separate the effects of Fe and Ni/Co on the spectrum. Also Cr and Ti have distinct effects: as long as their abundances are reasonably low, they suppress the UV flux without making strong features. Thus it was possible to determine the abundance of each element separately.

Five days later (-5.8 d, i.e. ~ 14.2 d after explosion), the SN had brightened significantly ($L_{\text{bol}} = 3.6 \times 10^9 L_{\odot}$), and the spectrum had become somewhat bluer (as indicated by the higher $T_{\text{ph}} = 13170\text{ K}$). The photosphere in our model recedes to 11400 km s⁻¹, and is located in a zone which is dominated by Si, but where also iron-group material is abundant. The UV feature at $\sim 3000\text{\AA}$ now has a stronger contribution of Fe III (and a large contribution by Si III), as the higher luminosity increases ionisation. Additionally, the feature at $\sim 3200\text{\AA}$, which was dominated by Ni II and Co II lines in the earlier spectrum, is now contaminated by

Fe III. Also, strong Co III lines begin to contribute there. Because of strong back-warming effects, Si is highly ionised and little Si II remains. Therefore, the Si II $\lambda 5972$ absorption (cf. Nugent et al. 1995; Hachinger et al. 2008) is weak. The O I $\lambda 7773$ feature is essentially missing for the same reason. We can also set rather stringent limits on the C content in the outer ejecta, as even small C abundances produce a visible C II $\lambda 6580$ line (which is not seen in the observations).

For epochs at *B*-band maximum and later, SN 2010jn displayed a normal SNIa spectrum. Our models have a bolometric luminosity $L_{\text{bol}} = 4.6 \times 10^9 L_{\odot}$ at -0.3 d and $L_{\text{bol}} = 4.0 \times 10^9 L_{\odot}$ at +4.8 d, respectively. The HVFs in Si II and Ca II have become much weaker, as it is the case in most SNe Ia. The model therefore fits the observations better and better with time. Even though the HVFs disappear, line velocities remain high compared to other SNe Ia. The photospheric velocity is $\sim 8850\text{ km s}^{-1}$ even around *B* maximum. At +4.8 d, the photosphere is at $\sim 7200\text{ km s}^{-1}$, and the photospheric temperature has dropped from $T_{\text{ph}} = 13450\text{ K}$ (the value at -0.3 d) to $T_{\text{ph}} = 12510\text{ K}$. High iron-group mass fractions ($\gtrsim 85\%$) are needed at $7200 < v < 11400\text{ km s}^{-1}$ in order to fit the low UV flux after maximum. These velocities are high, indicating efficient ^{56}Ni production and a luminous SN. The UV features after maximum are dominated by lines of Fe II ($\sim 3000\text{\AA}$) and Co III/Co II ($\sim 3200\text{\AA}$). Flux blocking around $\sim 2900\text{\AA}$ still is mostly due to Fe II and Mg II lines.

3.5.2 Shortcomings of the W7-based model

The major problem of the W7-based model is that the lines in the synthetic spectra at the earlier epochs generally do not reach velocities (blueshifts) as high as the observed features, although we adopted photospheric velocities as high as possible. This is a result of the steep decline of the W7 density at high velocities. The mismatch can be improved by assuming a delayed-detonation model (Sec. 3.6). We did not attempt to fit the HVFs, at this would require the density and/or electron density in the outermost zone to be enhanced probably by mixing with a circumstellar medium (Altavilla et al. 2007), which is beyond the scope of this paper.

Another notable shortcoming of the models is a lack of flux around 4000\AA , in particular at -10.5 d. The high flux in the observed -10.5 d spectrum may not be completely reliable (there is a sudden change with respect to -12.9 d), but more absorption in the Ca H&K feature would increase the re-emission into the peak.

Later synthetic spectra tend to show an excess of flux in the IR (redwards of $\sim 6500\text{\AA}$) compared to the observations. This is relatively independent of the assumed density model (cf. the WDD3-based models in Sec. 3.6). It is rather an artefact of using a black-

⁵ The $\sim 4700\text{\AA}$ trough is slightly too deep in the synthetic spectrum at this epoch; however, it is slightly too shallow at the next epoch.

⁶ The Ni/Co/Fe abundances are given in terms of the mass fractions of ^{56}Ni and stable Fe at $t = 0$ [$X(^{56}\text{Ni}_0)$, $X(\text{Fe}_0)$]; no stable Ni or Co and no radioactive Fe are assumed to be present, as these species – assuming realistic abundances – have less of an impact on our models.

body spectrum at the photosphere (Sec. 3.2.1). The resulting mismatch is however not expected to have major effects on our abundance determination. The fact that this happens so early suggests that the black body approximation fails earlier than in most SNe Ia. This is probably the consequence of the presence of significant amounts of ^{56}Ni near and above the photosphere even when the photospheric velocities are still high.

3.5.3 Abundance structure

The spectra probe the ejecta structure from the outermost layers down to 7200 km s^{-1} (+4.8 d photosphere). The abundances are shown and compared to the W7 nucleosynthesis in Fig. 5.

The model contains two zones with reduced abundances of burning products at $22000 \text{ km s}^{-1} \leq v \leq 33000 \text{ km s}^{-1}$ and $v > 33000 \text{ km s}^{-1}$. These are not strictly needed to improve the fit to the spectra, but were added in order to have a structure analogous with the WDD3-based models (see Sec. 3.6).

Moving inwards, there is a zone extending over $\sim 0.2 M_{\odot}$ ($14500 \text{ km s}^{-1} \lesssim v \lesssim 22000 \text{ km s}^{-1}$) which is dominated by O, but already contains a significant fraction of IME (Mg, Si and S) and iron-group elements.

IME clearly dominate in the velocity range $11000 \text{ km s}^{-1} \lesssim v \lesssim 14500 \text{ km s}^{-1}$ (i.e. over a mass range of $\sim 0.2 M_{\odot}$). Below $\sim 11000 \text{ km s}^{-1}$ (at a mass coordinate of $> 0.9 M_{\odot}$), where in most SNe Ia IME are still dominant (Mazzali et al. 2007), the ejecta of SN 2010jn begin to be dominated by iron-group material. This has only been seen in very luminous SNe Ia (Mazzali et al. 2007).

Comparing our tomography result with the W7 nucleosynthesis calculation (Fig. 5) reveals that iron-group elements are present in SN 2010jn at higher velocities. The higher burning efficiency is consistent with the luminosity (see also Stritzinger et al. 2006) and also with a high kinetic energy, as indicated by the high velocities in all spectral lines. Also with respect to other SNe studied with the tomography technique (e.g. Stehle et al. 2005; Tanaka et al. 2011; Mazzali et al. 2008; Hachinger et al. 2009), the SN shows a far more efficient burning. An additional difference is that SN 2010jn, unlike these other SNe, exhibits rather sharp transitions between the zones dominated by different elements (Fe-group, IME, C/O). This may have to do with the fact that in an efficiently burning SN Ia the zone in which IME are produced and the zone where O is left are constrained to relatively narrow outer shells, and less “mixing” is possible.

3.6 Models based on the WDD3 density

Having noticed the shortcomings of W7 as a backdrop density profile, we now test whether the spectra of SN 2010jn can be better fitted using the density of a delayed-detonation model. In a delayed detonation, an initial subsonic burning phase is followed by a phase of supersonic burning which more efficiently converts the original C/O mixture into processed elements (Khokhlov 1991). This type of explosion can produce a larger amount of iron-group elements as well as IME, and a higher kinetic energy, placing more material at high velocities. Although this scenario appears to be very promising for SNe Ia, the details of the transition from subsonic to supersonic burning are unfortunately still unclear.

Given the high luminosity of SN 2010jn and the efficient production of Fe group elements we find in our model, we use model WS15DD3 (in short WDD3), the brightest and most energetic of the WS15DD model series of Iwamoto et al. (1999).

Table 3. Luminosities, photospheric velocities and temperatures of the photospheric blackbody in the 10jn-WDD3 model.

Rest-frame phase (days)	L_{bol} ($10^9 L_{\odot}$)	v_{ph} (km s^{-1})	T_{ph} (K)
−12.9	0.75	14600	10220
−10.5	1.7	13350	11670
−5.8	3.5	11400	12830
−0.3	4.5	8850	13430
+4.8	4.0	7200	12700

WDD3 synthesizes $0.77 M_{\odot}$ of ^{56}Ni and has an explosion energy $E_{\text{kin}} = 1.43 \text{ foe}$.

For spectral modelling, the most important difference in the density structure of WDD3 in comparison to W7 (cf. Fig. 2) is the higher density in the outer part of WDD3.

In Fig. 6, our WDD3-based optimum models for SN 2010jn are compared to the data and to the W7-based models presented in the previous section.

3.6.1 Spectral models

The synthetic spectra we obtained using the WDD3 model reproduce the high line velocities of SN 2010jn significantly better [except for the HVF, which we do not attempt to reproduce – cf. Sec. 3.5 and Tanaka et al. (2011)]. At the earliest epochs, the larger extent of the line-forming zone in WDD3 (towards high velocities) makes the WDD3-based spectra smoother, which matches the observations much better. In particular, for the two earliest epochs (−12.9d, −10.5d), the fit to Si II $\lambda 6355$ and the Fe-dominated trough at $\sim 4700 \text{ \AA}$ are broader and give an improved fit over W7. The Ca II H&K features shows a significant improvement even at later epochs, and the flux at 4000 \AA matches the observations somewhat better. The UV region is matched just as well as in the W7-based model.

The improvements with respect to W7 are basically due to the higher density in the outer zones in the delayed-detonation model. The increased amount of material at high velocities enhances the absorption at larger blueshifts directly, but also through an indirect effect: the higher densities lead to a decreased ionisation, favouring singly-ionised species over doubly-ionised ones. As many important lines in SN Ia spectra are due to singly-ionised material, the blue line wings are better reproduced. However, apart from the outer layers, the changes in the model atmospheres from W7 to WDD3 are limited. This reflects in the fact that the optimum WDD3 model could be constructed using practically the same values for photospheric velocity and bolometric luminosity as for W7 (cf. Table 3). The photospheric black-body temperatures are similar to the W7-based models except for the first two epochs, where the WDD3-based models have a flatter temperature gradient because WDD3 has a lower density than W7 at $12500 \text{ km s}^{-1} \leq v \leq 16000 \text{ km s}^{-1}$ (cf. Fig. 2).

The UV features in the WDD3-based model at the earliest epochs are dominated by the same elements as in the W7-based model (Fe near $\sim 3000 \text{ \AA}$, Ni, and Co near $\sim 3200 \text{ \AA}$). At later times, all Fe-group elements contribute somewhat more to all features because of increased line opacities, but still the effects of the different Fe-group species are sufficiently distinct that the abundance of each element can be constrained.

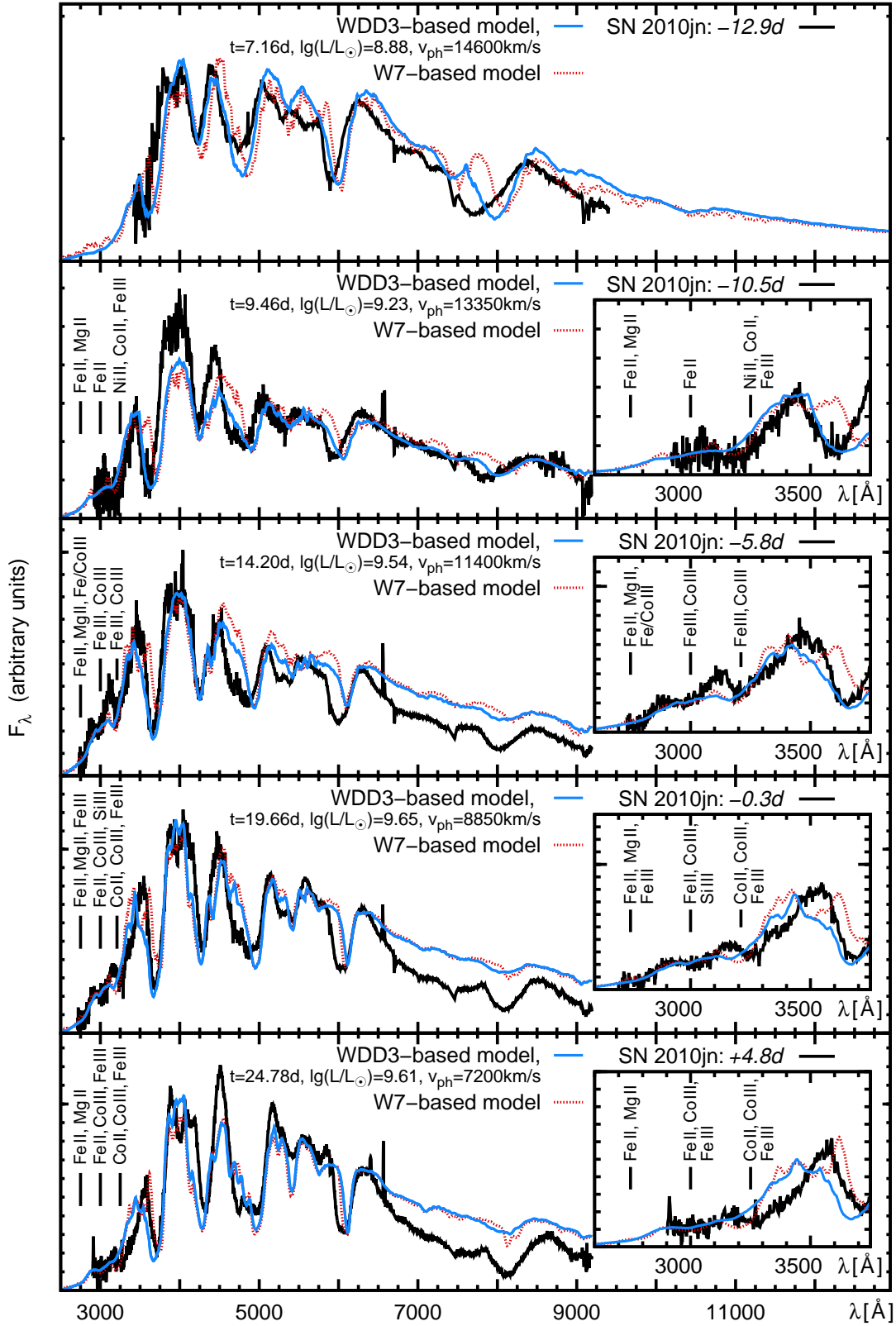


Figure 6. 10jn-WDD3 model sequence, based on the WDD3 density profile (light, blue lines). Observed spectra (black lines) and 10jn-W7 spectra from Fig. 4 (red, dotted lines) are given for comparison; insets show the UV in more detail. The differences in the density profile influence the line velocities. Observations and models are shown de-redshifted (i.e. in the SN's rest frame); no correction for host-galaxy reddening has been applied to the observed spectra [i.e. the models have been reddened by $E(B - V)_{\text{host}} = 0.36$ mag]. For the most prominent UV features, the respective ions dominating the absorption in our model are given (in order of importance). Note that Cr and Ti cause significant quasi-continuous absorption by a large number of weak lines, which are not reported here.

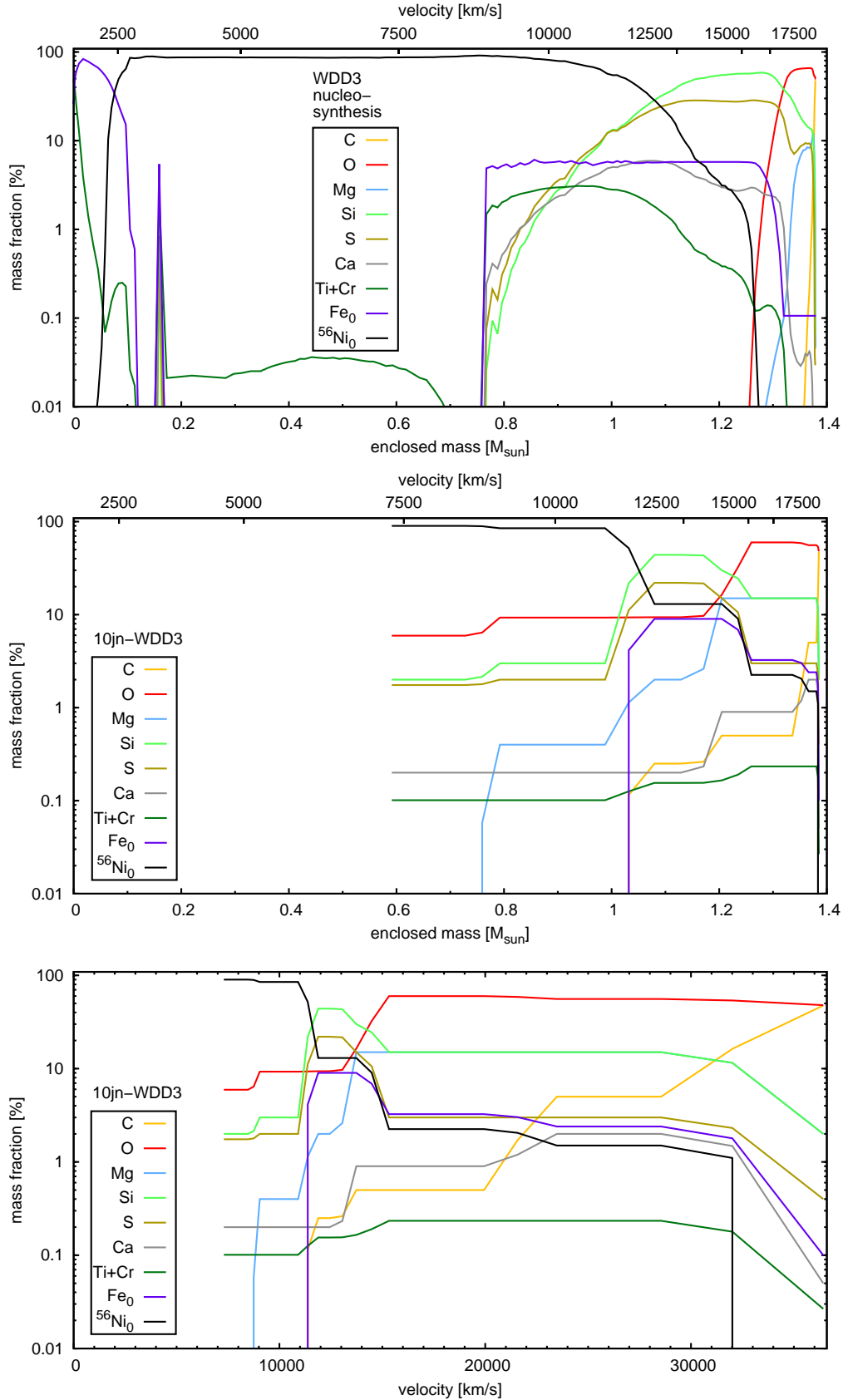


Figure 7. Abundances of WDD3 nucleosynthesis calculations (Iwamoto et al. 1999, *top panel*, plotted in mass space), compared to our tomography based on WDD3 (10jn-WDD3 model – *middle panel*: in mass space; *lower panel*: in velocity space). The C abundance in our model is an upper limit, as no C feature is present in the observations. The Ni/Co/Fe abundances are given in terms of the mass fractions of ^{56}Ni and stable Fe at $t = 0$ [$X(^{56}\text{Ni}_0)$, $X(\text{Fe}_0)$]; in our spectral models, no stable Ni or Co and no radioactive Fe are assumed to be present.

3.6.2 Abundance structure

In Fig. 7 we show the abundances of our 10jn-WDD3 model together with a plot of the original WDD3 nucleosynthesis. This model may be regarded as a reference for SN 2010jn: the good fits to the observed data indicate that the density of WDD3 provides a reasonable description to the actual ejecta. The abundance stratification of the WDD3-based models in velocity space is qualitatively similar to that of the W7-based models (3.5.3), despite the differences in the explosion models. Therefore, we can say that our results on the chemical structure should be reasonably independent of the density model.

In order to construct our optimum models, we have introduced two independent abundance zones in the outermost part of the ejecta ($22000 \text{ km s}^{-1} \leq v \leq 33000 \text{ km s}^{-1}$ and $v \geq 33000 \text{ km s}^{-1}$). These zones contain fewer burning products, ensuring optimum spectral fits (e.g. by avoiding spurious high-velocity absorption in the Fe/Mg feature at $\sim 4300 \text{ \AA}$). The Ca, Si and S abundances at $22000 \text{ km s}^{-1} \leq v \leq 33000 \text{ km s}^{-1}$ have been optimised to fit the higher-velocity parts of the respective features (except for the HVFs). Despite the decrease of most burning products (with respect to the lower layers), Ca and Ti/Cr remain abundant, possibly the result of incomplete burning.

Our model yields an upper limit of $\sim 60\%$ to the combined abundance of C and O at $14600 \text{ km s}^{-1} < v < 33000 \text{ km s}^{-1}$. With higher mass fractions, we would have lower fractions of burning products, and this would degrade the fit.

The moderate C/O abundance between 14600 and 33000 km s^{-1} is compensated by an IME mass fraction of $> 30\%$, a mass fraction of directly synthesised Fe of $\sim 3\%$, and a mass fraction of $\sim 2\%$ of ^{56}Ni and decay products. The UV spectra make it possible to disentangle the effects of Fe, ^{56}Ni and Ti/Cr, and to infer their respective abundances (see Fig. 7).

Assuming the WDD3 density profile, we have surveyed $0.8 M_{\odot}$ of the ejecta (down to the $+4.8 \text{ d}$ photosphere at 7200 km s^{-1}). The C/O content in this region is $\sim 0.15 M_{\odot}$. The mass in IME is $\sim 0.21 M_{\odot}$, and $\sim 0.45 M_{\odot}$ are in iron-group elements ($\sim 0.42 M_{\odot}$ in ^{56}Ni).

If the $\sim 0.6 M_{\odot}$ core, which cannot be analysed with our spectra, has a ^{56}Ni mass fraction as at our innermost photosphere (90%), SN 2010jn contains $0.9 M_{\odot}$ of ^{56}Ni . This is consistent with a very luminous SN Ia. In order to complete our analysis at the lowest velocities, nebular spectra would be required (cf. Mazzali et al. 2011).

Finally, comparing our abundance diagram with the delayed-detonation nucleosynthesis (Fig. 7), we find good agreement in the general structure with few exceptions. SN 2010jn shows somewhat more mixing than WDD3: in the IME-dominated zone, both oxygen and (to a smaller degree) iron-group elements are abundant.

A main finding of this analysis is the presence of burned material in the outer layers of SN 2010jn. The high iron-group abundances (Fe, Ti/Cr, ^{56}Ni) in these zones, which lead to a high total opacity of the ejecta, explain the large stretch of SN 2010jn. Evidence for ^{56}Ni out-mixing has already been given for the less energetic SN 2011fe (Nugent et al. 2011; Piro 2012), using different diagnostics.

3.7 The effect of iron-group material in the outer layers on the spectra

The determination of the abundances of different iron-group elements in the outer layers of SN 2010jn (Sections 3.5, 3.6) depends crucially on the early-time UV spectra.

To demonstrate this, we computed spectra using modified versions of our WDD3-based ejecta model (Fig. 8): we changed the iron-group abundances up and down by a factor of two in the outer layers above the -10.5 d photosphere (13350 km s^{-1}), where the ejecta are dominated by O and IME (cf. Fig. 7).

The earliest spectra (-12.9 d , -10.5 d) show a clear sensitivity of the UV flux on iron-group content, while changes in the optical are rather moderate. This is due to the fact that iron-group elements – apart from Fe itself – do not produce pronounced absorptions in the optical. Even the optical Fe lines are strongly blended with lines of other elements (Mg, Si). Therefore, the UV is the only reliable quantitative diagnostic of iron-group content in the outer ejecta.

At -5.8 d , the UV still reacts, but somewhat less, since the photosphere is located deep inside the region affected by the changes. The optical Fe lines again do not seem to react to metal content. The change seen in the Si II $\lambda 6355$ region is in fact due to a change in back-warming, which is however only an indirect and crude diagnostic for metal abundance.

At later epochs the UV spectra are more sensitive to the metal content in the inner layers. They remain practically unchanged when the outer zones are modified (Figure 8, lower two panels). They may be useful to diagnose the iron-group content in the core, which however can be better analysed using nebular-phase spectra.

4 SUMMARY AND CONCLUSIONS

We have used a well-established spectrum synthesis code to conduct, for the first time, Abundance Tomography with a series of photospheric UV/optical spectra of a SN Ia, SN 2010jn (PTF10ygu). The early observations have proved extremely valuable in order to constrain the iron-group content in the outer layers. Early UV spectra are probably the best diagnostics for this, as we have shown by recalculating our original models with modified iron-group abundances. The later spectra allow us to constrain the abundances further inwards and to obtain a comprehensive picture.

From our abundance analysis, we find that SN 2010jn was an energetic explosion with significant amounts of intermediate-mass and iron-group elements in the outer layers ($v > 13350 \text{ km s}^{-1}$). SN 2010jn has only a thin oxygen-dominated zone and a limited IME zone. Even these layers contain directly synthesised Fe ($\sim 0.01 M_{\odot}$) as well as ^{56}Ni and decay products (also $\sim 0.01 M_{\odot}$ in total). The presence of iron-group elements leads to a high opacity of the SN, consistent with the slow light-curve evolution. The UV spectra allowed us to determine the content of iron-group elements and to differentiate among them.

We favour for SN 2010jn a Chandrasekhar-mass delayed-detonation model (WDD3, Iwamoto et al. 1999). It allows us to reproduce the high expansion velocities in the observed spectra better than the ‘fast deflagration’ model W7 (Nomoto et al. 1984; Iwamoto et al. 1999), which has little material at high velocities.

The presence of Fe and ^{56}Ni in the outermost layers is not predicted by the original (1-D) WDD3 model. The abundance of Fe in the outer layers ($13350 \text{ km s}^{-1} \leq v \leq 33000 \text{ km s}^{-1}$) is between one and two orders of magnitude above solar. This can not come

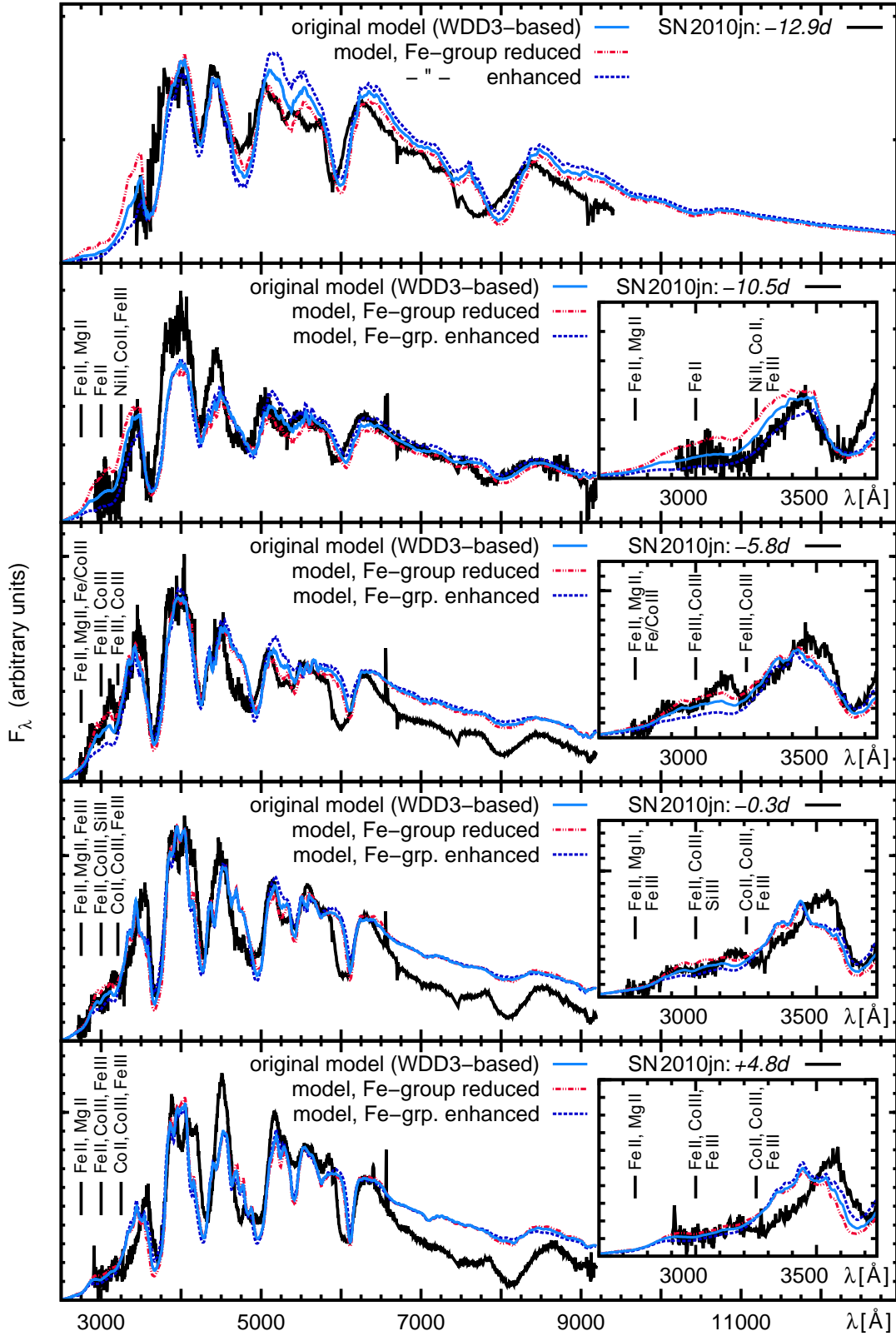


Figure 8. 10j-WDD3 model sequence (analogous to Fig. 6), and two versions of this sequence where the iron-group content at $v \gtrsim 13350 \text{ km s}^{-1}$ is reduced and enhanced by a factor of 2, respectively.

from the progenitor; it is rather a clue about the explosion properties of SN 2010jn. A high Fe-group abundance is consistent with an energetic SN, and the opacity due to Fe and ^{56}Ni in the outer layers explains the small decline rate of SN 2010jn. It is a challenge for explosion models to reproduce this. Multi-dimensional models may show some clumpiness or asymmetry which could appear to an observer as ‘outwards-mixing’ of iron-group material.

Our models favour a longer rest-frame rise time (~ 20 d) than predicted by the empirical τ^2 analysis of the early light curve (18.6 d). A longer rise time would imply that the SN after explosion has a ‘dark phase’ longer than predicted by the τ^2 (‘fireball’) model. SN 2010jn is more luminous than average SNe Ia: it remains to be seen whether the same phenomenon is found in other objects. Very early data are best suited to tackle this issue.

Finally, we remark that a precise analysis of the abundances in the outermost layers, as presented here, should be complemented by an analysis of the ejecta core, for which nebular spectra are necessary. Also, observations of more SNe Ia in the UV will be needed to establish the properties of the outermost layers of SNe Ia with different characteristics and light-curve properties.

ACKNOWLEDGEMENTS

This publication has been made possible by the participation of more than 10,000 volunteers in the Galaxy Zoo Supernovae project, <http://supernova.galaxyzoo.org/authors>. This work is based on observations made with the NASA/ESA Hubble Space Telescope, obtained at the Space Telescope Science Institute, which is operated by the Association of Universities for Research in Astronomy, Inc., under NASA contract NAS 5-26555. These observations are associated with program #12298. P.A.M. and S.H. acknowledge support by the programme ASI-INAF I/009/10/0. M.S. acknowledges support from the Royal Society, and A.G. acknowledges support by the ISF, a Minerva ARCHES award, and the Lord Sieff of Brimpton Fund. M.M.K. acknowledges generous support from the Hubble Fellowship and the Carnegie-Princeton Fellowship. We have used observations from the Liverpool Telescope, operated on the island of La Palma by Liverpool John Moores University in the Spanish Observatorio del Roque de los Muchachos of the Instituto de Astrofísica de Canarias with financial support from the UK Science and Technology Facilities Council. Spectroscopic observations in the optical have been taken at the Gemini Observatory under program ID GN-2010B-Q-13, which is operated by the Association of Universities for Research in Astronomy, Inc., under a cooperative agreement with the NSF on behalf of the Gemini partnership: the National Science Foundation (United States), the Science and Technology Facilities Council (United Kingdom), the National Research Council (Canada), CONICYT (Chile), the Australian Research Council (Australia), Ministério da Ciência, Tecnologia e Inovação (Brazil) and Ministerio de Ciencia, Tecnología e Innovación Productiva (Argentina). Finally, an optical spectrum has been taken at the WHT, operated on the island of La Palma by the Isaac Newton Group in the Spanish Observatorio del Roque de los Muchachos of the Instituto de Astrofísica de Canarias. We have used data from the NASA/IPAC Extragalactic Database (NED, <http://nedwww.ipac.caltech.edu>), operated by the Jet Propulsion Laboratory, California Institute of Technology, under contract with the National Aeronautics and Space Administration). For data handling, we have made use of various software (as mentioned in the text) including IRAF. IRAF – Image Reduction and Analysis Facility – is an astronomical data reduction soft-

ware distributed by the National Optical Astronomy Observatory (NOAO, <http://iraf.noao.edu>), operated by AURA, Inc., under contract with the National Science Foundation).

References

- Abbott D. C., Lucy L. B., 1985, *ApJ*, 288, 679
- Altavilla G., et al., 2007, *A&A*, 475, 585
- Barbon R., Rosino L., Iijama T., 1989, *A&A*, 220, 83
- Bessell M. S., 1990, *PASP*, 102, 1181
- Blondin S., Prieto J. L., Patat F., Challis P., Hicken M., Kirshner R. P., Matheson T., Modjaz M., 2009, *ApJ*, 693, 207
- Bongard S., Baron E., Smadja G., Branch D., Hauschildt P. H., 2008, *ApJ*, 687, 456
- Cardelli J. A., Clayton G. C., Mathis J. S., 1989, *ApJ*, 345, 245
- Conley A., et al., 2008, *ApJ*, 681, 482
- Cooke J. et al., 2011, *ApJ*, 727, L35
- Ellis R. S., et al., 2008, *ApJ*, 674, 51
- Filippenko A. V., et al., 1992, *AJ*, 104, 1543
- Foley R. J., Filippenko A. V., Jha S. W., 2008, *ApJ*, 686, 117
- Garavini G. et al., 2004, *AJ*, 128, 387
- Goldhaber G., et al., 1998, *BAAS*, 193, 47.13
- Hachinger S., Mazzali P. A., Tanaka M., Hillebrandt W., Benetti S., 2008, *MNRAS*, 389, 1087
- Hachinger S., Mazzali P. A., Taubenberger S. and Pakmor R., Hillebrandt W., 2009, *MNRAS*, 399, 1238
- Hamuy M., et al., 2002, *AJ*, 124, 417
- Hillebrandt W., Niemeyer J. C., 2000, *ARA&A*, 38, 191
- Hook I. M., Jørgensen I., Allington-Smith J. R., Davies R. L., Metcalfe N., Murowinski R. G., Crampton D., 2004, *PASP*, 116, 425
- Howell D. A., 2011, *Nature Communications*, 2, 350
- Hsiao E. Y., Conley A., Howell D. A., Sullivan M., Pritchett C. J., Carlberg R. G., Nugent P. E., Phillips M. M., 2007, *ApJ*, 663, 1187
- Iwamoto K., Brachwitz F., Nomoto K., Kishimoto N., Umeda H., Hix W. R., Thielemann F., 1999, *ApJS*, 125, 439
- Kessler R., et al., 2009, *ApJS*, 185, 32
- Khokhlov A. M., 1991, *A&A*, 245, 114
- Law N. M., et al., 2009, *PASP*, 121, 1395
- Lentz E. J., Baron E., Branch D., Hauschildt P. H., Nugent P. E., 2000, *ApJ*, 530, 966
- Lucy L. B., 1999, *A&A*, 345, 211
- Maguire K., et al., 2012, *MNRAS*, submitted (arXiv:1205.7040)
- Mazzali P. A., 2000, *A&A*, 363, 705
- Mazzali P. A., Benetti S., Stehle M., Branch D., Deng J., Maeda K., Nomoto K., Hamuy M., 2005, *MNRAS*, 357, 200
- Mazzali P. A., Lucy L. B., 1993, *A&A*, 279, 447
- Mazzali P. A., Maurer I., Stritzinger M., Taubenberger S., Benetti S., Hachinger S., 2011, *MNRAS*, 416, 881
- Mazzali P. A., Röpke F. K., Benetti S., Hillebrandt W., 2007, *Sci*, 315, 825
- Mazzali P. A., Sauer D. N., Pastorello A., Benetti S., Hillebrandt W., 2008, *MNRAS*, 386, 1897
- Nomoto K., Thielemann F., Yokoi K., 1984, *ApJ*, 286, 644
- Nugent P., Kim A., Perlmutter S., 2002, *PASP*, 114, 803
- Nugent P., Phillips M., Baron E., Branch D., Hauschildt P., 1995, *ApJ*, 455, L147
- Nugent P. E., Sullivan M., Cenko S. B., Thomas Kasen D., Howell D. A., Bersier D., Bloom J. S., et al., 2011, *Nature*, 480, 344
- Ofek E. O., et al., 2012, *PASP*, 124, 62

- Oke J. B., Gunn J. E., 1983, *ApJ*, 266, 713
 Pauldrach A. W. A., Duschinger M., Mazzali P. A., Puls J., Lennon M., Miller D. L., 1996, *A&A*, 312, 525
 Perlmutter S., et al., 1999, *ApJ*, 517, 565
 Phillips M. M., 1993, *ApJ*, 413, L105
 Phillips M. M., Lira P., Suntzeff N. B., Schommer R. A., Hamuy M., Maza J., 1999, *AJ*, 118, 1766
 Piro A. L., 2012, *ApJ*, submitted (arXiv:1201.5398)
 Poznanski D., Ganeshalingam M., Silverman J. M., Filippenko A. V., 2011, *MNRAS*, 415, L81
 Rau A., et al., 2009, *PASP*, 121, 1334
 Riess A. G., et al., 1998, *AJ*, 116, 1009
 Riess A. G., et al., 1999, *AJ*, 118, 2675
 Riess A. G., et al., 2007, *ApJ*, 659, 98
 Röpke F. K., Hillebrandt W., 2005, *A&A*, 431, 635
 Röpke F. K. et al., 2011, *Progress in Particle and Nuclear Physics*, 66, 309
 Sasdelli M., 2011, Master's thesis, Università di Pisa, Pisa, Italy
 Sauer D. N., et al., 2008, *MNRAS*, 391, 1605
 Schlegel D. J., Finkbeiner D. P., Davis M., 1998, *ApJ*, 500, 525
 Smith A. M., et al., 2011, *MNRAS*, 412, 1309
 Steele I. A., et al., 2004, in Oschmann Jr. J. M., ed., *Society of Photo-Optical Instrumentation Engineers (SPIE) Conference Series Vol. 5489 of Society of Photo-Optical Instrumentation Engineers (SPIE) Conference Series. The Liverpool Telescope: performance and first results.* pp 679–692
 Stehle M., Mazzali P. A., Benetti S., Hillebrandt W., 2005, *MNRAS*, 360, 1231
 Stritzinger M., Mazzali P. A., Sollerman J., Benetti S., 2006, *A&A*, 460, 793
 Sullivan M., et al., 2011, *ApJ*, 737, 102
 Tanaka M., Mazzali P. A., Stanishev V., Maurer I., Kerzendorf W. E., Nomoto K., 2011, *MNRAS*, 410, 1725
 Turatto M., Benetti S., Cappellaro E., 2003, in W. Hillebrandt & B. Leibundgut ed., *From Twilight to Highlight: The Physics of Supernovae Variety in Supernovae.* p. 200
 Walker E., et al., 2012, *MNRAS*, submitted
 Yaron O., Gal-Yam A., 2012, *PASP*, submitted (arXiv: 1204.1891)

APPENDIX A: CHOICE OF THE *B*-BAND RISE TIME

In order to calculate the models presented in the main text we have adopted a value of 20 d for the *B*-band rise time (in the rest frame of the SN). Here we discuss why we have chosen this rise time, which is a bit longer than the one which is inferred from the observations assuming a t^2 behaviour for the rising part of the light curve ($\tau_{r,\text{fire}} = 18.6$ d; Sec. 2.2).

During the process of modelling the SN, we have created various test models in order to determine which rise time allows for optimum models in terms of fit quality and physical consistency. Here, we show the differences between models assuming $\tau_{r,\text{fire}} = 18.6$ d and $\tau_r = 20$ d, which lead us to accept the latter value as the one more compatible with our models.

The fundamental difference when going from models with $\tau_r = 20$ d to models with a shorter rise time ($\tau_r = 18.6$ d) is the smaller size of the ejecta. This affects the expansion state of the ejecta, but also the radius of a photosphere located at a certain velocity v_{ph} . This affects the spectrum at the photosphere: a higher temperature T_{ph} is required to emit the same amount of radiation from a smaller photosphere.

To have photospheres at the same radius, keeping a similar

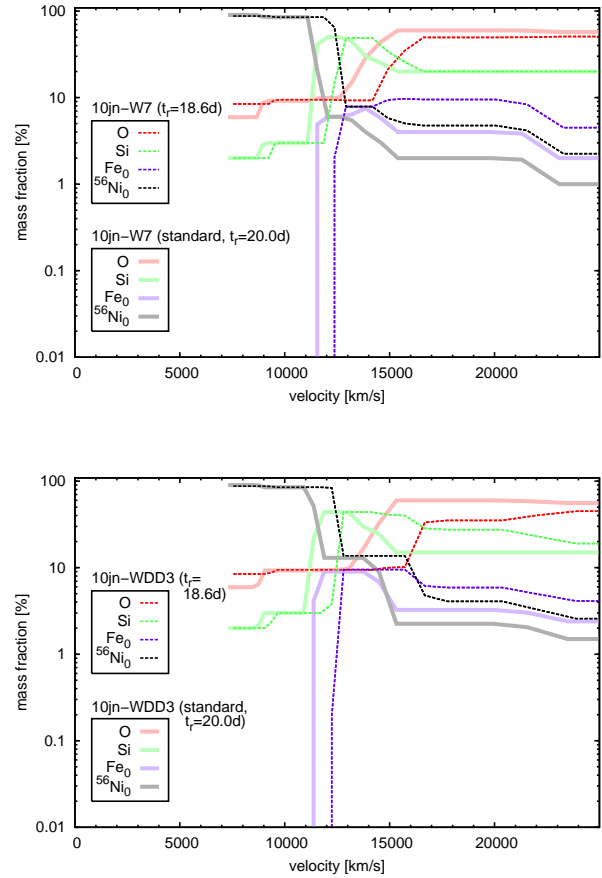


Figure A1. Distribution of the most abundant / relevant elements (in velocity space) in our $\tau_r = 18.6$ d models compared to the those in the standard ($\tau_r = 20$ d) models. *Top panel:* W7-based model; *bottom panel:* WDD3-based model. The black and violet graphs [mass fractions of ^{56}Ni and stable Fe at $t = 0$: $X(^{56}\text{Ni}_0)$, $X(\text{Fe}_0)$] give the abundances of the dominant iron-group elements, which are unrealistically high in the outer layers of the $\tau_r = 18.6$ d models (see text).

colour and temperature as in the $\tau_r = 20$ d model, a higher v_{ph} must be used if $\tau_r = 18.6$ d. For the earliest spectra (-12.9 d, -10.5 d), v_{ph} in our standard (20 d) model is already very high. An even higher velocity would mean that almost no mass is above the photosphere, but then line absorption would be reduced and it may then be difficult to reproduce the low observed UV flux (i.e. the flux in the model will be too high). The alternative would be to preserve the photospheric velocity from the standard calculation. In this case, however, the photospheric spectrum would be bluer (higher T_{ph} required to emit the same luminosity from a small-radius photosphere, as mentioned above). Again, one would be left with too much UV flux.

The only way to circumvent this and fit the observed spectra with $\tau_r = 18.6$ d is to use higher mass fractions of the iron-group elements in the outer ejecta in order to block the UV flux. Our standard ($\tau_r = 20$ d) models have already shown a relatively strong out-mixing of iron-group material (Sections 3.5.3, 3.6.2) with respect to the original W7/WDD3 models (Iwamoto et al. 1999). Assuming $\tau_r = 18.6$ d, the iron-group fractions in the outer layers are even higher and less realistic. The most relevant abundances in the $\tau_r = 18.6$ d and $\tau_r = 20$ d models are compared in Fig. A1. In the W7-based model with $\tau_r = 18.6$ d, an iron-group abundance

(sum of all iron-group elements) of $\sim 15\%$ is needed even above 15000 km s^{-1} . This is about twice the result of the explosive nucleosynthesis in the original W7 model (Iwamoto et al. 1999), which constitutes an inconsistency. In general, it will be difficult for most explosion models to produce high abundances of Fe-group material in the outermost layers: the densities there are small, leading to incomplete burning, and only “mixing” can bring burned material outwards. Our WDD3-based model shows a smaller effect, but still the high iron-group abundance in the outer layers of the $\tau_r = 18.6 \text{ d}$ model ($\sim 7\text{--}23\%$, with a stronger gradient than in the W7 case) leads us to prefer a rise time of $\gtrsim 20 \text{ d}$, for which the iron-group abundances in the outer layers of our models seem consistent with the WDD3 results if one assumes moderate additional out-mixing (cf. Sec. 3.6.2).

Models for UV observations at even earlier epochs would react even more sensitively to the assumed rise time. If earlier UV observations were available for SN 2010jn, a stricter lower limit on the rise time may have been determined through modelling. In order to exploit this possibility for future objects, we encourage UV observations of SNe Ia at epochs as early as possible.

